

Article

A Spatial and Temporal Correlation between Remotely Sensing Evapotranspiration with Land Use and Land Cover

Sajad Khoshnood¹, Aynaz Lotfata² , Maryam Mombeni³, Alireza Daneshi¹ , Jochem Verrelst^{4,*} 
and Khalil Ghorbani⁵

¹ Department of Watershed Management Sciences and Engineering, Gorgan University of Agricultural Sciences and Natural Resources, Gorgan P.O. Box 386, Iran; khoshnood@gau.ac.ir (S.K.); alireza.daneshi_s94@gau.ac.ir (A.D.)

² Department of Veterinary Pathology, School of Veterinary Medicine, University of California, Davis, CA 95616, USA; alotfata@gmail.com

³ Desert Affairs Office, Natural Resources and Watershed Management Organization, Tehran 1955756114, Iran; maryam.mombeni@gau.ac.ir

⁴ Image Processing Laboratory (IPL), Parc Científic, Universitat de València, 46980 Paterna, Spain

⁵ Department of Water Engineering, Faculty of Water and Soil Engineering, Gorgan University of Agricultural Sciences and Natural Resources, Gorgan P.O. Box 386, Iran; ghorbani.khalil@gau.ac.ir

* Correspondence: jochem.verrelst@uv.es

Abstract: In recent years, remote sensing technology has enabled researchers to fill the existing statistics and research gaps on evapotranspiration in different land use classes. Thus, a remotely sensed-based approach was employed to investigate how evapotranspiration rates changed in different land use/cover classes across the Lake Urmia Basin from 2016 to 2020. This was accomplished by applying the Surface Energy Balance System (SEBS) and the maximum likelihood algorithm. Results showed that from 2016 to 2020, grassland, savanna, and wetland decreased by 1%, 0.58%, and 1%, respectively, whereas an increase of 0.4%, 0.4%, 2.5%, and 1.2% occurred in cropland, urban, shrubland, and water bodies, respectively. Based on the model's results, over 98, 63, 90, 93, and 91% of the studied area, respectively, experienced a value of evapotranspiration between 0–6, 3–8, 0–4, 0–4, and 0–6 mm from 2016 to 2020. It was also found that these values are more closely related to water bodies and wetlands, followed by cropland, urban areas, savanna, non-vegetated, grassland, and shrubland. A strong correlation with $R^2 > 70\%$ was observed between the SEBS and the ground-measured values, while this value is lower than 50% for the MODIS Global Evapotranspiration Project (MOD16A2). The findings suggest that evapotranspiration and land use/cover can be extracted on a large-scale using SEBS and satellite images; thus, their maps can be presented in an accurate manner.

Keywords: actual evapotranspiration; Surface Energy Balance System; land use; Lake Urmia Basin



Citation: Khoshnood, S.; Lotfata, A.; Mombeni, M.; Daneshi, A.; Verrelst, J.; Ghorbani, K. A Spatial and Temporal Correlation between Remotely Sensing Evapotranspiration with Land Use and Land Cover. *Water* **2023**, *15*, 1068. <https://doi.org/10.3390/w15061068>

Academic Editor: Guido D'Urso

Received: 31 December 2022

Revised: 26 February 2023

Accepted: 8 March 2023

Published: 10 March 2023



Copyright: © 2023 by the authors. Licensee MDPI, Basel, Switzerland. This article is an open access article distributed under the terms and conditions of the Creative Commons Attribution (CC BY) license (<https://creativecommons.org/licenses/by/4.0/>).

1. Introduction

Considering the rate of evaporation and transpiration as one of the main components of the water balance is necessary for proper planning to improve the efficiency of water use in agriculture and water resources management [1]. In general, the process of evapotranspiration (ET) is defined as a combination of evaporation from the soil and plant surface and transpiration through the plant canopy [2,3]. ET is a flux that links the water and energy cycles of the biosphere, atmosphere, and hydrosphere. This interaction is critical in meteorology (simulation of atmospheric processes), hydrology (runoff prediction and groundwater level estimation), and agriculture (irrigation and tillage) [4,5]. Generally, it is divided into two main types: potential evapotranspiration (PET) and actual evapotranspiration (AET).

Assessing ET variations enables us to better understand the balance of energy flow and water [6]. This rate varies greatly in both space and time due to extensive spatial variation,

rainfall, soil hydrological behavior, vegetation types, and density [7–12]. ET is among the most difficult hydrological variables to quantify, and it is a challenging function to have an accurate assessment of its spatial average [13]. Generally, four approaches can be identified to calculate ET: (1) direct measurement such as using lysimeters, (2) hydrological methods such as running a water balance model, (3) meteorological methods such as using an energy balance model, and (4) empirical or combination methods [14]. These methods mostly provide a point estimation of ET based on energy or climatic factors, which certainly are not suitable for large-scale evaluation. Complexity in the hydrologic process and natural heterogeneity of the earth's surface as well as requirement of atmospheric factors to run them, limit these measurement techniques to be applicable on a wide scale [15]. Nowadays, by increasing applied remote sensing techniques in environmental modeling, it can provide the possibility of predicting ET using actual meteorological data and satellite imagery regional scale areas [16,17].

Earth observation (EO) technology has recently enabled the collection of regional data and the development of numerical climate models to study the actual evapotranspiration of the Earth's surface [4,18]. Covering a large area, frequent updates, and consistent quality are the main advantages of using them [19,20]. Accordingly, multiple algorithms based on meteorological input data and EO data have been developed to estimate evapotranspiration. Established methods include single-source models such as Surface Energy Balance Index (SEBI) [21], Surface Energy Balance Algorithm for Land (SEBAL) [21], Simplified Surface Energy Balance Index (S-SEBI) [22], Surface Energy Balance System (SEBS) [23], and Mapping Evapotranspiration at High Resolution and Internalized Calibration (METRIC) [24]; and two-source models such as Series Two-Source Energy Balance (S-TSEB) [25], and Parallel Two-Source Energy Balance (T-TSEB) [26,27].

Each of these models has varying degrees of accuracy depending on the input data type and quality, as well as their assumptions at various stages of development. The Surface Energy Balance System (SEBS) is one of the regional ET estimation models based on remote sensing techniques. It is a physical model with an appropriate scale that includes the physical state of the surface as well as aerodynamic resistances to estimate daily evaporation [28]. So, applying SEBS with the time series of the satellite imagery product is a successful procedure and was confirmed by several researchers [3,29–32].

Furthermore, as a hydrological component, the AET variable is closely related to changes in land use/cover (LULC) [33].

For energy balances and a proper understanding of regional hydrological cycles, the distinct effects of land-use change on ET must be quantified [30]. This ensures superior performance and conservation of ecosystem services and efficient water resource management [34]. Hence, a wide range of studies were dedicated to calculating EO-based data for ET and LULC classification worldwide [1,18,21,30,35–38]. For instance, Li et al. [30], used MODIS data products to evaluate the impact of LULC and climate changes on ET in China from 2001–2013. Outcomes revealed that from 2001 to 2013 the annually ET decreased by 0.6 mm. The SEBAL model was used by Chemura et al. [1] in order to estimate interception, transpiration, and ET contributions in the Buzi basin in Zimbabwe. Results showed that the highest amounts of ET where the land cover type named tea had the highest water interception rate. Among the climatic factors, sunshine duration, and wind speed, as well as LULC, the reduction in forest area had the greatest impact on ET. However, climate change impacted ET more than LULC changes overall. Gibson et al. [39] conducted a review of energy balance methods in South Africa, concluding that the SEBAL model is the most widely used, but they also highlighted the potential of the SEBS model. It was recommended by them that any future research on the SEBS model in South Africa should be limited to agricultural areas with accurate vegetation parameters, high-resolution imagery with low sensor zenith angles, and complete canopy coverage. There have also been a number of studies demonstrating biases in the use of MODIS data to estimate evapotranspiration. For example, Srivastava et al. [40] and Autovino et al. [41] used MODIS data to estimate evapotranspiration. Based on the results, the MODIS-ET

values are highly underestimated with periodic shifts. The shadows cast by leaves and cloud cover were considered responsible for this underestimation. It is noteworthy that the use of different models to measure ET is associated with uncertainties that can affect the management of water resources [42]. According to Jung et al. [43], land surface models and diagnostic ET datasets were compared and uncertainty was calculated as the standard deviation of the differences between grid cells within the image, and the sensitivity of the inputs such as meteorological forcings and land cover types were also studied. Overall, the literature review confirms that the use of MODIS data in tandem with actual measured data is capable of providing more accurate estimates of evapotranspiration.

Shortage or unavailability of water in arid and semi-arid regions such as Iran is becoming a serious issue, and because of this, estimation of AET is a key function to water resources management. The Lake Urmia Basin (LUB) as a semi-arid area located in the northwest of Iran, is currently facing major problems such as population growth, industrial development, high use of river water, high evaporation rate, and continuous salt deposition, which has resulted in Lake Urmia's high salinity [44]. Changes in LULC classes in this region, such as dam construction, water diversion, and rangeland degradation, can exacerbate these issues. If the process of exploiting water resources and making inappropriate land use decisions is not controlled, the lake gradually shrinks.

Although a range of studies have classified land classes and derived ET based on EO data in the LUB [44–46], most of these studies focused on the search of the potential ET and some specific land types such as agricultural lands in this basin. There are only a few studies that analyzed the variation in actual ET regarding LULC classes in this basin. Therefore, in this research, a remote sensing model (SEBS) is used to retrieve the AET in the LUB from 2016 to 2020, with the results being validated with a MODIS product named MOD16A2. Then, LULC classes are detected and categorized using the maximum likelihood algorithm. This study also seeks to answer the following questions: (1) Which LULC classes have the greatest impact on AET value in the LUB? (2) How do different land use/cover classes affect the SEBS and MODIS production models? In general, it can be acknowledged that the general purpose of the present study is to investigate the changes in the amount of evapotranspiration in different LULC classes by using satellite images. It is important to note that two main reasons motivated the selection of the LUB as the case study. The first issue is that there have been few studies on the hydrology system and climatic conditions within the basin until now. Secondly, there are very limited hydrological and meteorological data for this basin, as well as poor quality and gaps in the data.

The remainder of this paper is structured as follows. Section 2 describes the SEBS model, MOD16A2, and LULC extraction, as well as how they are implemented. Section 3 describes the SEBS model execution results and extracted LULC maps and compares the outputs of SEBS and MOD16A2 in distinct LULC classes. The fourth section looks at the relationship between LULC changes and retrieved AET values from the SEBS, MOD16A2, and measurement gauges. Section 5 concludes the paper with the study's findings.

2. Materials and Methods

2.1. Study Area Description

The LUB is located northwest of Iran at an altitude of 1274 m. Lake Urmia is the second largest saltwater lake in the world [47] and also the largest inland lake in Iran with an area of 51,800 km². According to the latest divisions of the country, this lake is divided between the two provinces of East Azerbaijan and West Azerbaijan and is located between the longitude of 44 to 48 degrees east and the latitude of 35 to 38.5 degrees north (Figure 1). The length of the lake is 130 km to 146 km². The width is 15 to 58 km². This basin, with plains such as Tabriz, Urmia, Maragheh, Mahabad, Miandoab, Naqadeh, Salmas, Piranshahr, Azarshahr, and Oshnoyeh, is an important area for agricultural and livestock activities in Iran. This is one of Iran's six major basins, and its altitude ranges from 1280 to 3600 m AMSL [48]. This lake has 102 small and large islands and an average depth of about 6 m [37].

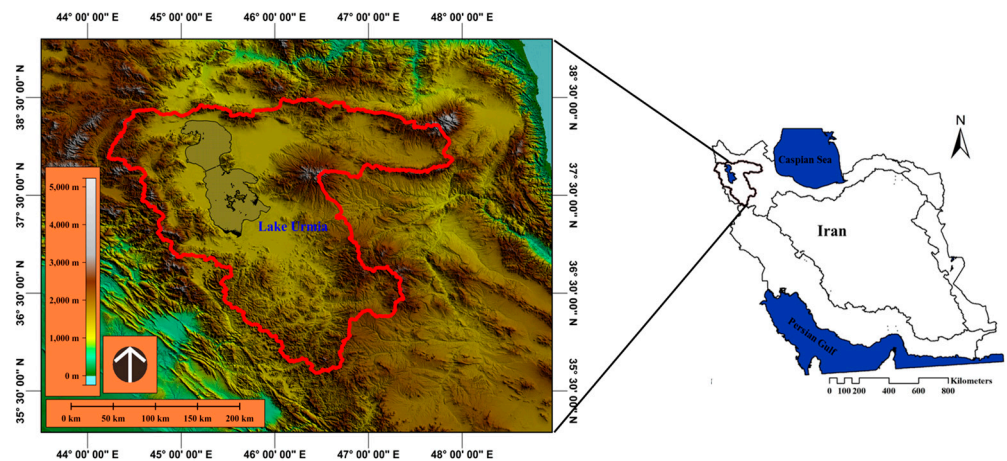


Figure 1. Location of LUB in Iran.

2.2. Research Methods

Classifying LULC types and observing their impacts on the rate of AET includes the following steps: (1) data collection (collect ET data from four gauge stations) and image pre-processing (Operational Land Imager (OLI) Landsat 8 and MOD16A2 product with a 30 and 500 m spatial resolution, respectively), (2) extract LULC classes using the maximum likelihood algorithm based on satellite imagery and then estimate AET values based on the SEBS model, and finally (3) assess the relationship between different estimation sources of AET (ground-measured values, the SEBS model, and the MOD16A2 product). All these steps are illustrated in Figure 2, and all used data are listed in Table 1.

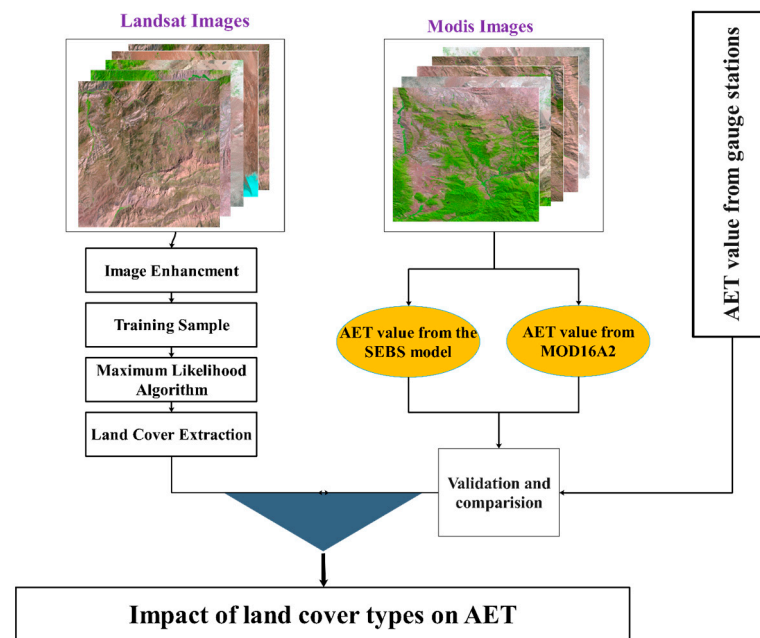


Figure 2. Data processing diagram.

Table 1. Data description used in this study.

Data Type	Dataset	Date	Source Reference	Band Number	Calculation Method	
Satellite images	Landsat	Landsat 8 OLI	14 June 2016	WGS84	2,3,4,5	-
		(path/row: 168/33,	14 June 2017	-	-	
		169/33, 168/34, 169/34,	14 June 2018	-	-	
		and 168/35, 169/35	14 June 2019	-	-	
			14 June 2020	-	-	
	MODIS	MOD021KM, MOD16A2, MOD03	14 June 2016	WGS84	1,2,3,4,5,7, 17,18,19,31,32	-
			14 June 2017	-	-	
			14 June 2018	-	-	
			14 June 2019	-	-	
			14 June 2020	-	-	
Evaporation	Ground gauge	From 8th June to 14th June of each year	Point data	-	Accumulative	
Precipitation	Ground gauge	From 8th June to 14th June of each year	-	-	Accumulative	
Temperature	Ground gauge	From 8th June to 14th June of each year	-	-	Average	

2.2.1. Image Preprocessing

Because of the area size of the basin, six landsat images with different paths and rows for each year (from 2016 to 2020) including 168/33, 169/33, 168/34, 169/34, 168/35, and 169/35 and MODIS images were acquired through the United States Geological Survey (NASA Earth data search n.d.). To reduce the effect of seasonal and phenological changes, the images were selected on 14 June for all years studied with less than 5% cloud cover [49]). The Fast Line-of-sight Atmospheric Analysis of Hypercubes (FLAASH) pattern and Iteratively Reweighted Multivariate Alteration Detection (IR-MAD) were respectively used for atmospheric and radiometric corrections. As seen in Table 1, UTM was used as the coordinate system in all images data in this study. All processes were performed with ENVI software version 5.4.

2.2.2. Land Use/Cover Classification

Following image correction, LULC types were classified into eight major groups: (1) croplands, (2) grasslands, (3) non-vegetated, (4) savannas, (5) shrublands, (6) urban areas, (7) water bodies, and (8) wetlands (presented in Table 2). Then, using ENVI software version 5.4, training points were chosen for each of those classes based on land cover information. To extract and classify LULC maps, the maximum likelihood algorithm was used. The main classification technique for land remote sensing imagery in this algorithm is calculating the probability of a pixel belonging to each land cover class and then dividing it into the most probable category. The ability to interpret parameters, simple implementation, and easy fusing with prior knowledge are the main advantages of this method [44,50–52].

Table 2. Visual characteristics of the areas to assess accuracy in the LUB source area.

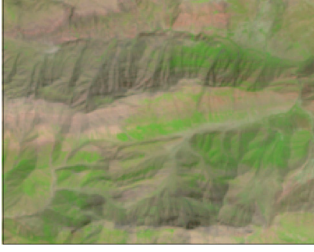
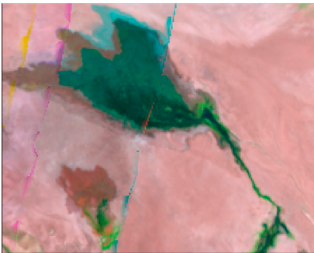
LULC	Interpretation Criterion	Image	Photograph
water bodies	At least 60% of area is covered by permanent water bodies		
Shrublands	Dominated by woody perennials (1–2 m height) 10–60% cover		
Savannas	Tree cover 10–30% (canopy > 2 m)		
Grasslands	Dominated by herbaceous annuals (<2 m)		
Wetlands	Permanently inundated lands with 30–60% water cover and >10% vegetated cover		
Croplands	At least 60% of area is cultivated cropland		

Table 2. Cont.

LULC	Interpretation Criterion	Image	Photograph
Urban	At least 30% impervious surface area including building materials, asphalt and vehicles		
Non-Vegetated	At least 60% of area is non-vegetated barren (sand, rock, soil) or permanent snow and ice with less than 10% vegetation		

2.2.3. The SEBS Model Description

Su [23] developed the SEBS algorithm for estimating heat flux by combining satellite data and meteorological field data. This algorithm, as demonstrated by van der Kwast and de Jong [53], can accurately estimate atmospheric turbulence flux and surface evaporation from a single point to the continental scale. The SEBS includes a set of tools for measuring spectral reflectance and radiation to determine the physical parameters of the land surface, such as temperature, albedo, emissivity, brightness temperature, and vegetation coverage [23]. It estimates the actual daily ET by calculating the energy required to change the water phase from liquid to gas using remote sensing and meteorological data [39].

Earth's energy budget (EEB) is usually referred to as a balance between the energy coming into the Earth system from the Sun at the top-of-atmosphere (TOA)—denoted as incoming shortwave radio reflux F_0 —against energy lost to space that consists of reflected shortwave (F_s) and emitted long-wave (F_l) radiative fluxes. EEB at the TOA, often called energy imbalance, can be characterized by net radiation between incoming (F_0) and outgoing radiative fluxes (F_s and F_l) accounting for the remainder of the Earth system—land surfaces, oceans, and atmosphere:

$$F_n = F_0 - F_s - F_l = F_0(1 - a_{TOA}) - F_l \quad (1)$$

where a_{TOA} is the planetary albedo, or Bond albedo, defining the fraction of incident global mean shortwave radiative flux reflected to space [54].

According to Su [23], the surface energy balance can be expressed as Equation (2). All required data in the equation were extracted from the landsat metadata file of each year:

$$R_n = G_0 + H + \lambda E \quad (2)$$

Here, R_n is the net radiation, G_0 is the soil or water heat flux, H is the sensible heat flux, and λE is the latent heat flux (λ is the latent heat of vaporization and E is the actual evapotranspiration). The net radiation is calculated using Equation (3):

$$R_n = (1 - \alpha) \cdot R_{swd} + \varepsilon \cdot R_{lwd} - \varepsilon \cdot \sigma \cdot T_0^4 \quad (3)$$

Here α is the albedo, R_{swd} is the downward solar radiation, R_{lwd} is the downward longwave radiation, ε is the surface emissivity, σ is the Stefan-Boltzmann constant, and T_0 is the surface temperature in Kelvin.

The soil or water heat flux is calculated using Equation (4):

$$G_0 = R_n \cdot [\Gamma_c + (1 - f_c) \cdot (\Gamma_s - \Gamma_c)] \quad (4)$$

In this equation, Γ_c the ratio of soil heat flux to net radiation for dense vegetation is considered to be 0.05. Γ_s The ratio of soil heat flux to net radiation for bare soil is considered to be 0.315. f_c is a partial canopy coverage that can be calculated using remote sensing data.

Energy balance at limiting cases is used to calculate the evaporation fraction. The evaporation fraction in SEBS is obtained using the sensible heat flux. Under dry conditions the latent heat flux is minimal and can be ignored, in which case the energy balance equation can be summed as Equation (5):

$$\lambda E_{dry} = R_n - G_0 - H_{dry} = 0, \text{ or} \quad (5)$$

$$H_{dry} = R_n - G_0$$

In wet conditions, the actual evapotranspiration reaches the potential evapotranspiration, in this case we obtain (Equation (6)):

$$\lambda E_{wet} = R_n - G_0 - H_{wet}, \text{ or} \quad (6)$$

$$H_{wet} = R_n - G_0 - \lambda E_{wet}$$

Then the energy balance mode on dryness and wetness is used to estimate the relative evaporation fraction (Λ_r), as in Equation (7):

$$\Lambda_r = 1 - \frac{H - H_{wet}}{H_{dry} - H_{wet}} \quad (7)$$

The evaporation fraction is estimated from Equation (8):

$$\Lambda = \frac{\lambda E}{R_n - G_0} = \frac{\Lambda_r \cdot \lambda E_{wet}}{R_n - G_0} \quad (8)$$

The daily evaporation can be expressed as Equation (9):

$$E_{daily} = \lambda E / \lambda \rho_w \quad (9)$$

Here, E_{daily} is the daily evaporation ($\text{mm} \cdot \text{day}^{-1}$); PW is the water density ($\text{kg} \cdot \text{m}^{-3}$); λE latent heat ($\text{W} \cdot \text{m}$).

In this study, the SEBS model has been run with inputs derived from a MODIS image and meteorological field data.

2.2.4. MOD16A2 AET Product

The NASA MOD16A2 product provides 500-m 8-day global ET estimates extending. The product was collected from the NASA Earth data search website (NASA Earth data search n.d.), as the dataset: "MODIS/Terra Net Evapotranspiration 8-Day L4 Global 500 m SIN Grid V006". The function of this product is based on the Penman–Monteith equation (NASA Earth data search n.d.). Since the primary estimated values of this product range between $-32,767$ to $32,700$ for a region, those values certainly required to be corrected regarding the defined scale factor (this scale is 0.1 for ET). Thus, to gain the real value of ET, the value of each pixel was multiplied by 0.1 (as the scale factor). Missing values of this range were filled using the local mean of a 3 by 3-pixel window. These processes were executed in ENVI 5.4.

3. Results

3.1. Land Use/Cover Assessment

Figure 3 shows the spatial pattern of LULC types. It can be stated that for every 5 years studied, the area of the water bodies class has increased with a certain trend. So, its area was estimated as 4.7 percent (2515.4 km²) of the total basin area in 2016, while it reached 5.9 percent (3166 km²) in 2020. Wetlands have had a downward trend in the same period, so in 2016 it was approximately 2.97 percent (1592.3 km²) of the total LUB area, then it reached around 1.93 percent (1033.5 km²) in 2020. Grasslands covered about 43% (23,304 km²) and 42% (22,723.6 km²) of the whole basin in 2016 and 2020, respectively. Shrublands coverage has decreased in the years 2017 and 2019, whereas its area has increased in the years 2018 and 2020. In 2016, this coverage was estimated as 7% (3750.4 km²), and in 2020, 9.5% (5126 km²) of the whole basin area. The savanna area in the years 2017, 2018, and 2019, respectively, 0.70% (369.3 km²), 0.40% (208 km²), and 0.72% (387.6 km²), compared to 2016 (8.58 %, 4596.6 km²) has increased, while in the year 2020, its area decreased by 0.5% (270 km²) and reached 4226 km² (8% of the total basin area). Urban areas have had an upward trend over the same period, so in 2016, the area was estimated at 7.8%, while in 2020 it was estimated at 8.2%. The study of non-vegetated lands showed a decrease in the area by 2.5%, which was equal to 1350.5 km², between 2016 and 2020. Croplands with an area of 8908.7 km² (16.6%) in the year 2016 have reached an area of 9120.1 km² (17%) in the year 2020, which indicates an increase in the area of this land cover class, and this change is equal to 0.4% of the area. As a result, based on the above statistics, the most extensive types of LULC are grassland, cropland, savannas, and non-vegetated, respectively.

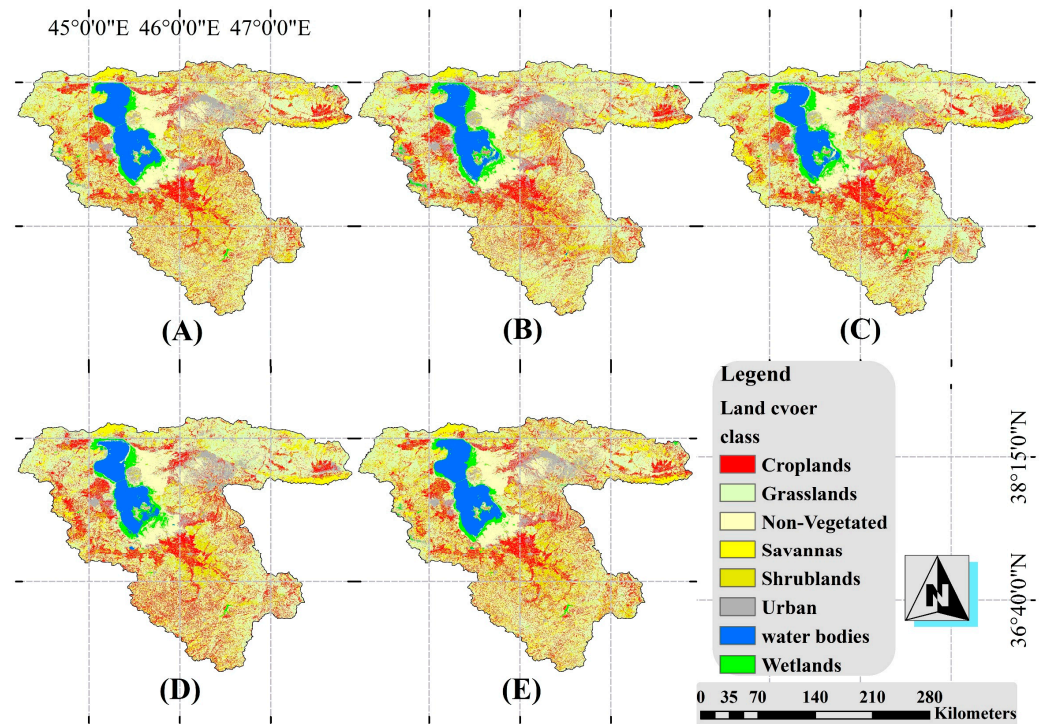


Figure 3. Spatial pattern of extracted LULC types in the LUB for the years 2016 (A), 2017 (B), 2018 (C), 2019 (D), and 2020 (E).

The confusion matrix was used to estimate the accuracy of the maximum likelihood classification method. For this purpose, several samples for each land class were selected from Google Earth, and then the overall accuracy (OA) was applied between these samples and their corresponding points on the extracted LULC maps. About sixty-five samples were randomly selected for each of the eight categories as a validation sample. Finally, the

overall classification accuracy based on the OA in 2016, 2017, 2018, 2019, and 2020 was estimated at 86, 89.6, 92.7, 90, and 83.2 percent, respectively (Table 3).

Table 3. Classification accuracy verification values.

Year	LULC Class	Water Body	Shrub Land	Savanah	Grassland	Wetland	Cropland	Urban	Non-Vegetated	Overall Accuracy
2016	Produce's Accuracy (%)	96.6	67.4	75	79.3	93.4	68.8	67.2	80.5	86
2017	Produce's Accuracy (%)	98.3	76.3	72.8	72.1	95.7	68.5	70.3	83.6	89.6
2018	Produce's Accuracy (%)	98.7	72.5	77.9	74.6	94.6	68.8	73.4	79.6	92.7
2019	Produce's Accuracy (%)	99.1	76.7	74.1	72.3	95.8	66.2	72.4	82.7	90
2020	Produce's Accuracy (%)	96.5	73.6	69.3	74.4	96.2	66.4	65.8	78.6	83.2

3.2. Retrieval AET from the SEBS

Actual evapotranspiration estimated based on the SEBS algorithm for the years 2016, 2017, 2018, 2019, and 2020 is presented in Figure 4. The developed maps showed temporal and spatial variations in the AET rate inside the basin. Spatial variations are primarily due to changes in LULC types, plant types in arable lands, and plant cultivation dates. In contrast, temporal changes can result from changes in air temperature and vegetation density in different years. As shown in Figure 4A,B, the AET with higher values were in 2016 and 2017 as we moved northward in the basin. In Figure 4A, 51% of the area experienced AET values in the range of 0 to 4 mm, 48% had 3 to 6 mm, and only 1% had 6 to 8 mm. In 2017 (Figure 4B), 51% of the region had AET values between 3 to 6 mm, and 12% had 6 to 8 mm. In 2018 (Figure 4C) and 2019 (Figure 4D), the amount of AET decreased so that more than 90% of the region experienced values between 0 to 4 mm. In 2020 (Figure 4E), we observed an increase in this amount, so 59%, 32%, and 9% of the region had values between 0 to 4 mm, 3 to 6 mm, and 6 to 8 mm, respectively. These substantial spatial changes in AET values from distinct years but at the same date would be justified only by considering climate variables such as temperature and precipitation, as shown in Figure 5. In the years 2018 and 2019, the rate of temperature has relatively raised by 2 °C compared to the other years. Likewise, the average amount of precipitation in these years has fallen and was recorded close to zero for the whole area. Thus, regardless of each land class's effect, any changes in climate variables would affect the AET value. Additionally, Figure 6 shows the changes in monthly precipitation and temperature versus ET variation.

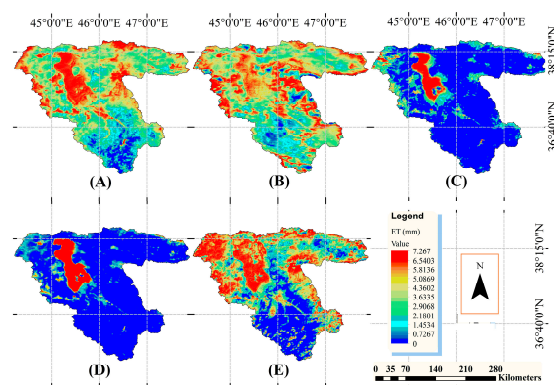


Figure 4. Spatial pattern of AET values estimated using SEBS model across the LUB for the years 2016 (A), 2017 (B), 2018 (C), 2019 (D), and 2020 (E).

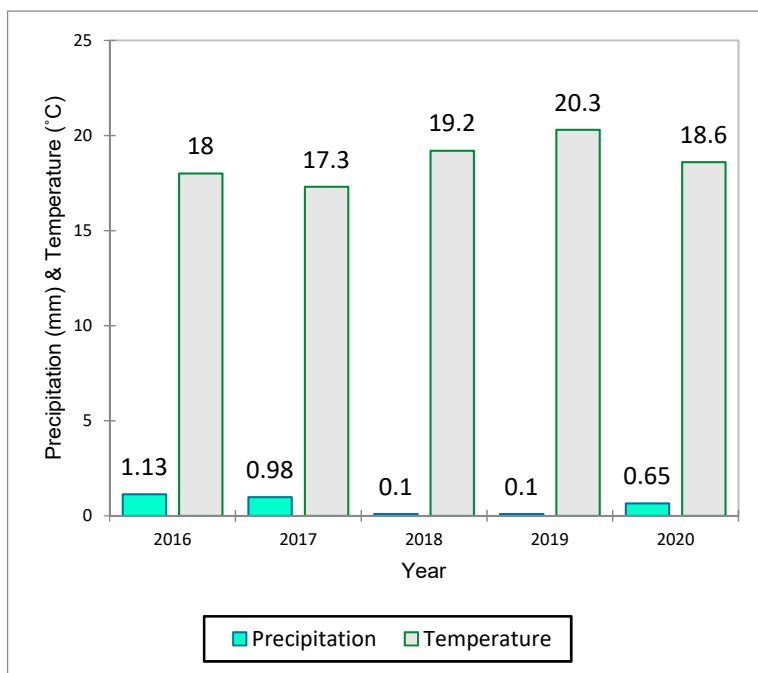


Figure 5. Accumulative amount of precipitation and average temperature in the LUB from 8/June to 14/June for years 2016, 2017, 2018, 2019, and 2020.

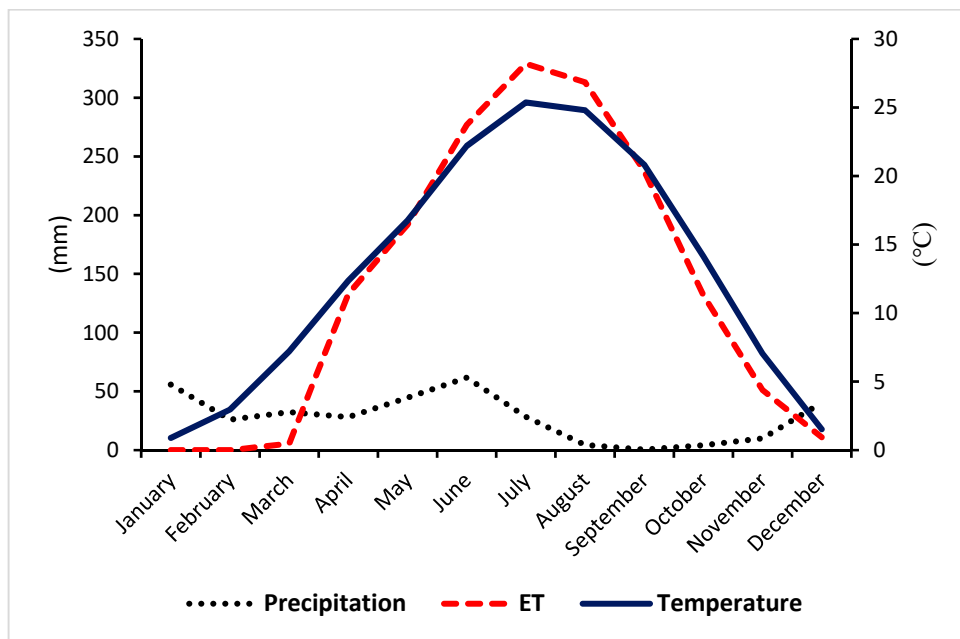


Figure 6. Changes in monthly average of precipitation and temperature versus ET variations Figure 7 shows the area changes in AET values in different years. Graphs for 2016 and 2017 revealed that all LULC classes experienced a high amount of AET. Due to seasonal rains, some moisture in soil layers has evaporated. However, in 2018 and 2019, hot and dry conditions prevailed, and there was no water for evaporation. The graph for the year 2020 shows the minimal amount of AET. In all years, the corresponding graph shows an increased value of AET in the range of 5 mm to 7 mm, which is related to water bodies and wetlands.

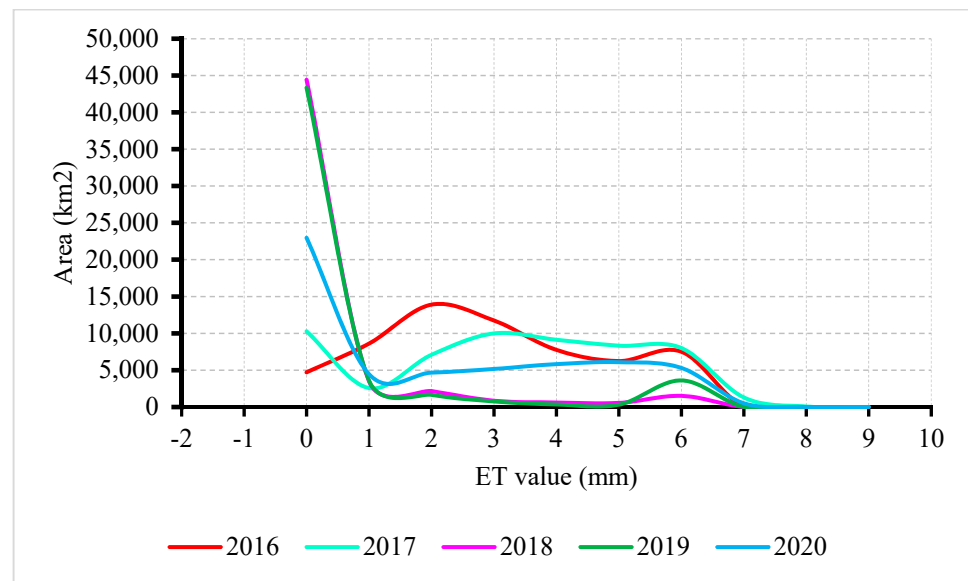


Figure 7. Area changes in AET from SEBS model during 2016 to 2020 in the LUB.

3.3. AET and LULC Relationship

Figure 8 illustrates the variation in actual evapotranspiration throughout distinct LULC types. The horizontal axis shows different land classes, and the left vertical axis shows the percentage of evapotranspiration volume based on the area of each class and the percentages of the LULC classes' areas. On the opposite side, the vertical axis presents the ratio of the percentage of AET to the percentage of each LULC area specified. As shown in the Figure, the type of LULC with water bodies and wetlands has the lowest percentage of the area (0.06% and 0.03%). Their total volume of evapotranspiration is also low (0.12 and 0.03). However, the ratio of evapotranspiration to the percentage of area in these types of LULC compared to other LULC types has the highest amount because of the presence of water (1.99 and 1.65). Savannas, solitary trees, and shrubs have more water in their plant fibers than grassland and annual plants. Therefore, the ratio of evapotranspiration to the percentage of area in this type of LULC is also high (1.13). In cropland, the high ratio of evapotranspiration to the percentage of area is due to irrigation (1.27). Urban areas have hand-planted trees and urban water drainage canals, so increasing the evapotranspiration ratio to the area percentage is close to the average (1.16). Another class, which is called non-vegetated, cannot establish any plant due to its vicinity to the lake and high salinity. However, because of the high level of groundwater, the evapotranspiration rate is high compared to the percentage of this land class (0.92). Most of the areas are covered by grassland, so the percentage of area under the denominator is a large number. On the other hand, it seems that at the date the image was taken, grassland had little or dried vegetation, so the ratio of evapotranspiration to the percentage of area decreased. Given the results, the rate of AET is more related to water bodies and wetland types, followed by cropland, urban areas, savanna, non-vegetated, grassland, and shrubland.

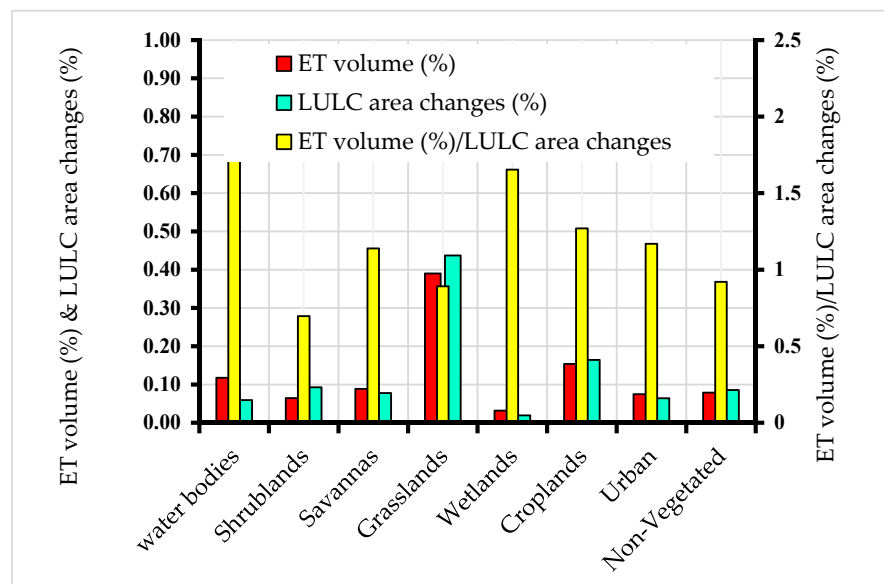


Figure 8. AET volume (%), the percent area of each LULC type, and the relationship between them in the LUB.

Figure 9 provides the amount of AET differences between selected LULC classes from northwest to southeast of the Lake Urmia Basin. As shown in Figure 9, water bodies and wetlands are marked with blue and green dots at their highest level on the graph, while the areas around these classes indicate lower AET values. The red dots indicate croplands. As stated in the Figure 8 description, due to farming practices and irrigation, the amount of AET in these parts is higher than that in urban and non-vegetated areas. The figure clearly reveals a high rate of AET in the areas where water bodies, wetlands, and agricultural land are prevalent. Likewise, it shows a low rate of AET in regions covered by grassland and savanna.

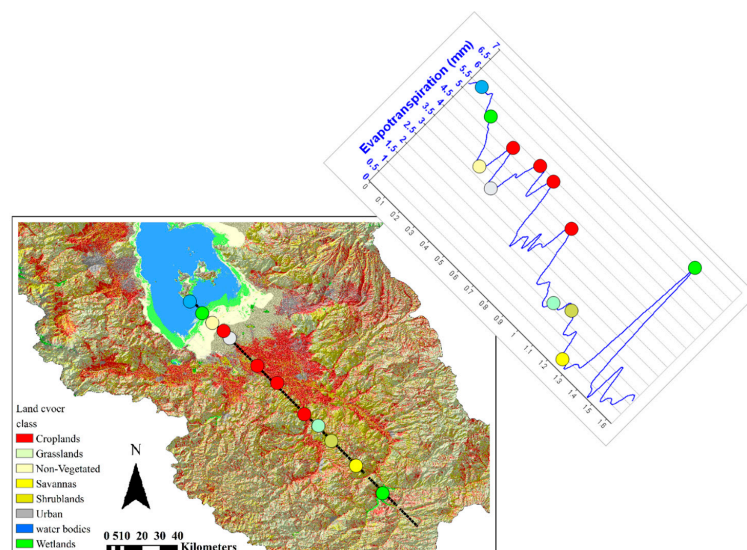


Figure 9. Change in estimated AET value using SEBS model while it is passing over different land cover LULC types in the LUB.

3.4. Comparison of AET Values Obtained in Different LULC Types

The output of both SEBS and MOD16A2 models was compared with the ground measured values of AET, and their correlations were evaluated using two methods of ordinary least square (OLS) and geographically weighted regression (GWR) [55] (see

Table 4). Based on the table, R^2 obtained from both GWR and OLS methods is more than 70% for the SEBS model, while less than 50% for MOD16A2. Likewise, R^2 estimated in GWR is more significant than its value in the OLS method for both models.

Table 4. Comparison of SEBS output model, MOD16A2 data, and ground measured data (mm) in the LUB.

Station Name	2016	2017	2018	2019	2020	R2 (GWR)	R2 (OLS)
gauge #A	5.6	5.3	1.8	4.3	1.1	-	-
SEBS model	4.7	4.4	2	5.4	2.2	0.779	0.741
MOD16a2	7.9	9.9	8.6	7.4	4.2	0.404	0.434
gauge #B	4.9	3.9	4.3	2.1	3.8	-	-
SEBS model	4.2	4.3	3.8	2.5	4.3	0.732	0.712
MOD16A2	9.3	6.9	5.3	3.9	9.4	0.470	0.435
gauge #C	2.1	4.8	1.6	0.3	4.2	-	-
SEBS model	1.8	4.5	0.9	0.8	4.7	0.968	0.846
MOD16A2	6.3	8.9	5.7	6.2	6.4	0.509	0.476
gauge #D	4.8	5.1	4.9	4.4	6.3	-	-
SEBS model	5.2	5.5	4.2	3.7	6.4	0.767	0.713
MOD16A2	6.7	7.4	4.3	7.3	9.2	0.365	0.370

The descriptive correlations derived from the SEBS and MOD16A2 model estimates computed using different land cover classes in the LUB are given in Figure 10. From the figure, the SEBS vs. MOD16A2 performed well for the wetlands ($r = 0.89$), croplands ($r = 0.74$), shrub lands ($r = 0.67$), and water bodies ($r = 0.66$). Likewise, results showed a weak performance in this comparison for the grassland class ($r = 28$). It is notable that the MODIS product calculates relatively higher AET values compared to the SEBS model, especially for some LULC classes such as savanna and grassland, which suggests the weak performance of MOD16A2 in an arid region as opposed to the SEBS model.

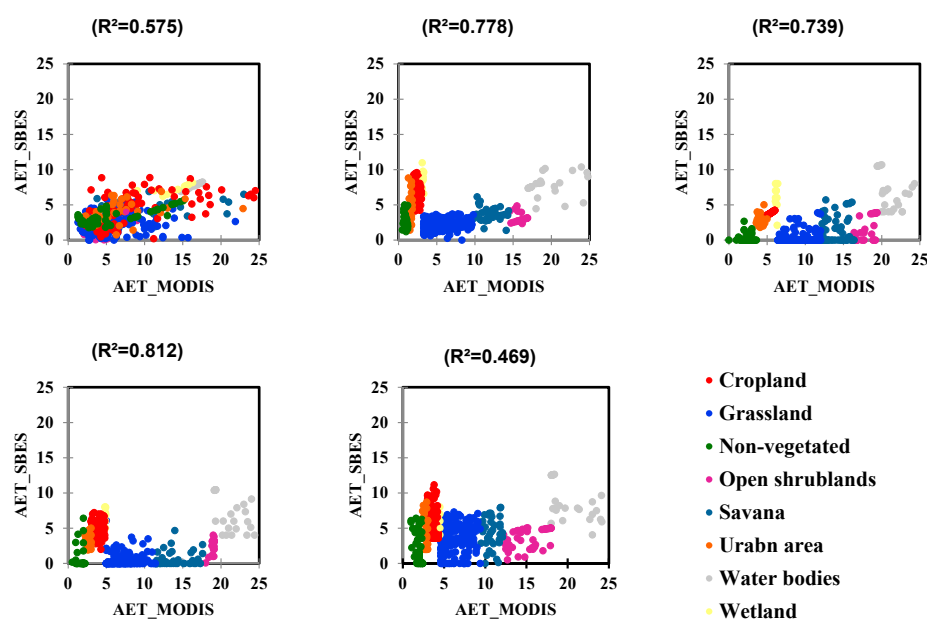


Figure 10. Comparison of estimated AET of the SEBS and MOD16A2 models across different land use/cover types from 2016 to 2020.

Lastly, we focused on the differences that appeared between the SEBS model, MOD16A2, and observed AET values; the simulated values from each of them were visualized for 2017 (Figure 11). Figure 11B reveals that many small and large areas (black colors) cannot be simulated with MOD16A2. These areas mostly include water bodies, lakes, and snow-capped mountains due to the lack of vegetation cover. Another slip that can be obtained from the figure is an overestimation of MOD16A2 (Figure 11B). This overestimation is well observed in vegetated areas, and it had been simulated as 10 times greater than the SEBS simulated values in some places.

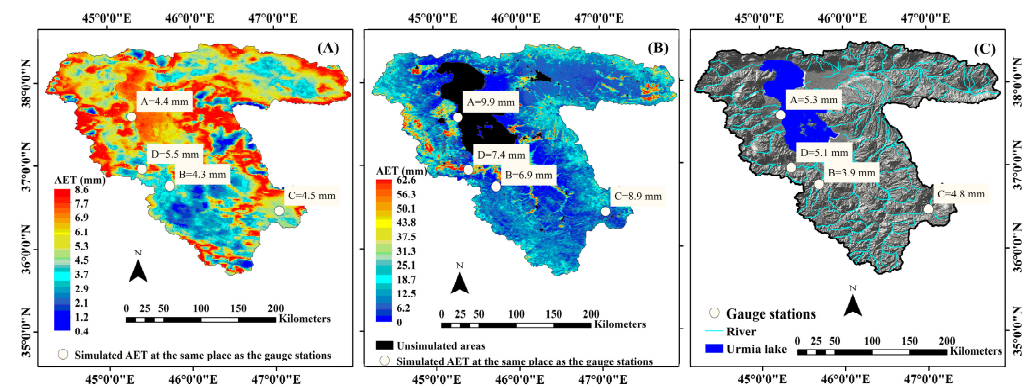


Figure 11. Visualization of estimated and observed AET in the LUB for the SEBS (A), MOD16A2 (B), and gauge stations (C) for 14 June 2017.

4. Discussion

This study used the SEBS algorithm to determine the actual evapotranspiration rate for each land use/cover class in the Lake Urmia Basin using MODIS and Landsat images. Most areas had an AET value between 0 and 4 mm in 2016, 2018, 2019, and 2020, while a large percentage of the basin had an AET value between 3 and 6 mm in 2017. Because the study area is in an arid and semi-arid region, the rate of AET varies from year to year and does not follow a consistent pattern. This rate can be affected by rainfall and cropland irrigation, as W Senkondo, Tumbo, and Lyon [2] predicted that cropland evapotranspiration would increase due to rain-fed irrigation.

Distinct land cover types were classified using the maximum likelihood algorithm from 2016 to 2020, and their accuracy was assessed by applying a confusion matrix. The highest and lowest OA of this classification are calculated in 2018 and 2020 with 92.7% and 83.2%, respectively. Based on the findings, OA values for water bodies and wetlands are higher than the values in the other classes, particularly in croplands and urban areas. Overall, according to the results obtained from all land classes (OA > 83%), it can be concluded that the accuracy level for extracting and classifying LULC maps in this study area is acceptable. Based on the extracted maps (Figure 2), grassland is the dominant land cover in the basin, with an average area of 23,685 km² (44% of the total basin area). Cropland is the second most common type of LULC, accounting for approximately 9000 km² (16% of the total basin area) and mostly located around the lake. According to the findings, grassland and cropland areas decreased and increased by approximately 580 km² and 210 km², respectively, from 2016 to 2020, with cropland increasing being the primary reason for grassland reduction. These findings are consistent with those of Farokhnia, Moradi, and Delvar [56] as well as Kamali and Yunes zadeh [57]. From 2016 to 2020, the area of water bodies and urban areas increased slightly, while the size of wetlands decreased slightly.

We found a significant relationship between LULC types and AET values which is in agreement with past studies [30,33,37,55]. As shown in Figure 7, the ratio of AET to area in grassland is lower than in other LULC classes, particularly in water bodies and wetlands. This is due to the date of the images used in the study and the evaporating water in the land at the time. This figure also reveals an increase in AET for areas with irrigation crops

or bodies of water. The majority of the energy available in these areas is spent on the AET process, resulting in a decrease in temperature in these areas (the results are not presented). In addition to other environmental factors, the effect of LULC on actual evapotranspiration can be evaluated by analyzing changes in surface temperature. Pourmohammadi et al. [58] also demonstrated that differences in evapotranspiration caused by different land classes resulted in significant changes in surface temperature. Although the percentage of area in water bodies and wetlands is the lowest, the ratio of AET to the percentage of area in these classes is the highest compared to other classes due to the presence of water. Thus, given the question “which LULC classes have the major impact on AET value in LUB?”, our findings indicated that the highest AET values were observed for wetlands and water bodies, and the lowest levels were observed for grassland and shrub land areas, respectively. Eventually, the findings of this section confirm earlier studies that reported different AET rates between land classes [33,36,38].

AET estimates are driven by a temporal distribution that is characterized by seasonal changes in potential evaporation and water resource availability. As a result, AET estimates for a specific land cover type may deviate from the natural distribution over time. Other factors, such as the topography of a land class, may influence the distribution of values within the same land cover class. Therefore, SEBS and MOD16A2 production models were compared to determine how the SEBS and MODIS production models react to different LULC classes. On the same time scale, the results indicated that the SEBS model had a higher capacity than the MOD16A2, so that both ordinary least square (OLS) and geographically weighted regression (GWR) estimated $r^2 > 70$ and $r^2 < 50$ for these models, respectively; these results are in line with Jahangir and Arast [59]. The SEBS model, for example, performed well in estimating AET in some LULC classes, such as water bodies, wetlands, cropland, and shrublands, whereas MOD16A2 overestimated AET in these classes. Furthermore, MOD16A2 levels in savanna and grassland classes were substantially higher than those measured on the ground. This model also has a low spatial resolution, so in some cases, the low resolution of input data can play a significant role in evaluating results [55].

The study’s findings revealed that the type of LULC and the rate of change for each land class are the main non-climatic factors influencing AET value at different scales. Although some earlier studies have investigated ET variations versus LULC in this basin [49,51,52], they mostly evaluated potential ET and specifically interpreted a few general land types. However, determining different values of actual ET regarding different LULC types with a precise categorization is the advantage of this research. Meanwhile, both anthropogenic and natural resources should be considered to observe changes in evapotranspiration, and such models should probably be coupled with climate or atmospheric models to obtain more accurate feedback. In other words, accurate information about land layers is necessary to achieve a better estimate of the AET rate, and coupling a LULC change model with such models is essential for a reasonable prediction of the future that takes into account climatic factors such as precipitation and temperature. This study provides an entry point for LULC changes and how to affect the AET rate. As a result, the findings of this study should be interpreted as a means of discussing and raising awareness of the effects of LULC changes for policy makers and planners in Lake Urmia Basin, the basin which is susceptible to any anthropogenic activity.

5. Conclusions

This study aimed to investigate remotely sensing-derived evapotranspiration and its spatial and temporal correlation with land use and land cover. As such, land classes were divided into eight main categories. OA for this classification was estimated more than 83.2%, for all the studied years. Therefore, given the achieved results, we conclude that the accuracy of extracting and classifying LULC maps is acceptable. It was observed that from 2016 to 2020, the spatial variations in the LULC types were found to be as follows; grassland changed from 43% to 41%, cropland was 17% to 15%, savanna and non-vegetated was 8%

to 7%, urban and shrub land was 7% to 9%, water bodies 4% to 5%, and wetland was 2% to 1.5%. Results also revealed that the most extensive LULC types are grassland, cropland, and shrubland, respectively. Most area changes were taking place in shrubland, with a ~1375 km² area, followed by non-vegetated water bodies and grassland. Our findings suggest that about 98% of the studied area experienced values between 0–6 mm in the year 2016. Likewise, over 63%, 90%, 93%, and 91% of the region have experienced values between 3–8, 0–4, 0–4, and 0–6 mm in years 2017, 2018, 2019, and 2020, respectively. Comparing AET values to LULC types, the changes revealed that the rate of AET is mostly associated with water bodies and wetland types, followed by cropland, urban areas, savanna, non-vegetated, grassland, and shrub land. R² of the SEBS model for both the ordinary least square and geographically weighted regression methods was over 70%, while it was less than 50% for MOD16A2. Hence, the results indicate a more accurate correlation between the SEBS output and the measured ground values as opposed to the MOD16A2. Our results also revealed that the AET in some land cover classes, such as savanna and grassland areas, is more than the real values, which indicates a weak performance of MOD16A2 vs. the SEBS model in a semi-arid area.

Assessment of spatial changes in AET between different LULC types is a reliable way to understand how to manage each pixel of land in order to mitigate this rate of evapotranspiration. Additionally, the methods employed here for point-based (stationary) AET calculation enable each user to compute AET, and the spatial distribution and zoning of AET in a region map would certainly allow for spatial water management. This will be a step forward in terms of water conservation and allocation to each basin area.

As a result of comparing the present study with previous similar studies, it is evident that, unlike previous studies that examined the changes in ET primarily in a few land use classes, the present study examined the changes in ET in all land use classes while extracting land use classes with high accuracy. Another important point is that the present study did not limit itself to satellite data and compared the results obtained from the SEBS model and the MOD16A2 product with observational five-year data by preparing ground data. It should also be noted that the SEBS model is also a relatively new model that was developed with the development of remote sensing technology and has only received special attention in studies of recent years. All these things can be stated as innovations of the present study.

To summarize, although land cover types and land-use practices impose a significant impact on the change in actual evapotranspiration, meteorological dynamics such as precipitation and temperature play a more decisive role in determining the rate of evapotranspiration in the LUB. Additionally, we strongly recommend considering other climatic parameters for the modeling and predicting of ET in the study area for future studies. In addition, the present study was limited by the lack of available data for a longer period of time. Consequently, in future research, in selecting the study area, care should be taken to ensure that sufficient meteorological stations and actual data are available for extended periods. The availability of observed data for a longer period will also provide the possibility of conducting research similar to the current research but with more reliable outcomes.

Author Contributions: Conceptualization, S.K. and A.D.; methodology, S.K.; software, S.K.; validation, S.K.; formal analysis, S.K.; investigation, S.K. and A.D.; resources, M.M.; data curation, S.K.; writing—original draft preparation, M.M. and, J.V.; writing—review and editing, S.K., A.D. and A.L.; visualization, S.K.; supervision, A.L. and K.G.; project administration, J.V.; funding acquisition, J.V. All authors have read and agreed to the published version of the manuscript.

Funding: J.V. was funded by the European Research Council (ERC) under the ERC-2017-STG SENTIFLEX project (grant agreement 755617) and Ramón y Cajal Contract (Spanish Ministry of Science, Innovation and Universities).

Data Availability Statement: Not applicable.

Conflicts of Interest: The authors declare no conflict of interest.

References

- Chemura, A.; Rwasoka, D.; Mutanga, O.; Dube, T.; Mushore, T. The impact of land-use/land cover changes on water balance of the heterogeneous Buzi sub-catchment, Zimbabwe. *Remote Sens. Appl. Soc. Environ.* **2020**, *18*, 100292. [[CrossRef](#)]
- Senkondo, W.; Tumbo, M.; Lyon, S.W. On the Evolution of Hydrological Modelling for Water Resources in Eastern Africa. *Remote Sens.* **2018**, *11*, 1–26. [[CrossRef](#)]
- Tian, X.; Van der Tol, C.; Su, Z.; Li, Z.; Chen, E.; Li, X.; Yan, M.; Chen, X.; Wang, X.; Pan, X.; et al. Simulation of Forest Evapotranspiration Using Time-Series Parameterization of the Surface Energy Balance System (SEBS) over the Qilian Mountains. *Remote Sens.* **2015**, *7*, 15822–15843. [[CrossRef](#)]
- Li, Z.L.; Tang, R.; Wan, Z.; Bi, Y.; Zhou, C.; Tang, B.; Zhang, X. A Review of Current Methodologies for Regional Evapotranspiration Estimation from Remotely Sensed Data. *Sensors* **2009**, *9*, 3801–3853. Available online: <https://www.mdpi.com/1424-8220/9/5/3801> (accessed on 19 May 2009). [[CrossRef](#)] [[PubMed](#)]
- Zhigang, S.; Wang, Q.; Batkhishig, O.; Ouyang, Z. Relationship between Evapotranspiration and Land Surface Temperature under Energy- and Water-Limited Conditions in Dry and Cold Climates. *Adv. Meteorol.* **2016**, *2016*, 55386680. [[CrossRef](#)]
- Pan, X.; Liu, S.; Yang, Y.; You, C.; Yang, Z.; Xie, W.; Li, T. Spatio-Temporal Characteristics of the Evapotranspiration in the Lower Mekong River Basin during 2008–2017. *Remote Sens.* **2022**, *14*, 2609. Available online: <https://www.mdpi.com/2072-4292/14/11/2609> (accessed on 29 May 2022). [[CrossRef](#)]
- Aguilos, M.; Stahl, C.; Burban, B.; Hérault, B.; Courtois, E.; Coste, S.; Bonal, D. Interannual and Seasonal Variations in Ecosystem Transpiration and Water Use Efficiency in a Tropical Rainforest. *Forests* **2018**, *10*, 14. Available online: <https://www.mdpi.com/1999-4907/10/1/14> (accessed on 26 December 2018). [[CrossRef](#)]
- Christoffersen, B.O.; Restrepo-Coupe, N.; Arain, M.A.; Baker, I.T.; Cestaro, B.P.; Ciais, P.; Saleska, S.R. Mechanisms of water supply and vegetation demand govern the seasonality and magnitude of evapotranspiration in Amazonia and Cerrado. *Agric. For. Meteorol.* **2014**, *191*, 33–50. [[CrossRef](#)]
- Liu, Q.; Wang, T.; Han, Q.; Sun, S.; Liu, C.Q.; Chen, X. Diagnosing environmental controls on actual evapotranspiration and evaporative fraction in a water-limited region from northwest China. *J. Hydrol.* **2019**, *578*, 124045. [[CrossRef](#)]
- Ma, N.; Zhang, Y.; Guo, Y.; Gao, H.; Zhang, H.; Wang, Y. Environmental and biophysical controls on the evapotranspiration over the highest alpine steppe. *J. Hydrol.* **2015**, *529*, 980–992. [[CrossRef](#)]
- Marques, T.V.; Mendes, K.; Mutti, P.; Medeiros, S.; Silva, L.; Perez-Marin, A.M.; Bezerra, B. Environmental and biophysical controls of evapotranspiration from Seasonally Dry Tropical Forests (Caatinga) in the Brazilian Semi-arid. *Agric. For. Meteorol.* **2020**, *287*, 107957. [[CrossRef](#)]
- Rubert, G.C.D.; de Arruda Souza, V.; Zimmer, T.; Veeck, G.P.; Mergen, A.; Bremm, T.; Roberti, D.R. Patterns and Controls of the Latent and Sensible Heat Fluxes in the Brazilian Pampa Biome. *Atmosphere* **2021**, *13*, 23. Available online: <https://www.mdpi.com/2073-4433/13/1/23> (accessed on 24 December 2021). [[CrossRef](#)]
- Nouri, H.; Beecham, S.; Kazemi, F.; Hassanli, A.M.; Anderson, S. Remote Sensing Techniques for Predicting Evapotranspiration from Mixed Vegetated Surfaces. *Hydrolo. Earth Syst. Sci. Discuss.* **2013**, *10*, 3897–3925. Available online: <https://www.hydrolo-earth-syst-sci-discuss.net/10/3897/2013/> (accessed on 25 March 2013). [[CrossRef](#)]
- Thomthwaite, C.W.; Mather, J.R. Instructions and tables for computing potential evapotranspiration and the water balance. *Publ. Climatol.* **1957**, *10*, 185–310.
- DeBruin, H.A.R. Time to Think: Reflections of a Pre-Pensioned Scintillometer Researcher. *Bull. Am. Meteorol. Soc.* **2009**, *90*, 17–26. [[CrossRef](#)]
- Jin, X.; Zhu, X.; Xue, Y. Satellite-Based Analysis of Regional Evapotranspiration Trends in a Semi-Arid Area. *Int. J. Remote Sens.* **2019**, *40*, 3267–3288. [[CrossRef](#)]
- Sun, R.; Gao, X.; Liu, C.M.; Li, W.X. Evapotranspiration Estimation in the Yellow River Basin, China Using Integrated NDVI Data. *Int. J. Remote Sens.* **2004**, *25*, 2523–2534. [[CrossRef](#)]
- Senkondo, W.; Munishi, S.E.; Tumbo, M.; Nobert, J.; Lyon, S.W. Comparing Remotely-Sensed Surface Energy Balance Evapotranspiration Estimates in Heterogeneous and Data-Limited Regions: A Case Study of Tanzania’s Kilombero Valley. *Remote Sens.* **2019**, *11*, 1289. Available online: <https://www.mdpi.com/2072-4292/11/11/1289> (accessed on 30 May 2019). [[CrossRef](#)]
- Cleugh, H.A.; Leuning, R.; Mu, Q.; Steven, W. Running. Regional Evaporation Estimates from Flux Tower and MODIS Satellite Data. *Remote Sens. Environ.* **2007**, *106*, 285–304. [[CrossRef](#)]
- Wang, K.; Wang, P.; Li, Z.; Cribb, M.; Sparrow, M.A. simple method to estimate actual evapotranspiration from a combination of net radiation, vegetation index, and temperature. *J. Geophys. Res. Atmos.* **2007**, *112*, 1–14. [[CrossRef](#)]
- Bastiaanssen, W.G.M.; Menenti, M.; Feddes, R.A.; Holtslag, A.M. A remote sensing Surface Energy Balance Algorithm for Land (SEBAL): 1. Formulation. *J. Hydrol.* **1998**, *213*, 198–212. [[CrossRef](#)]
- Roerink, G.J.; Su, Z.; Menenti, M. S-SEBI: A Simple Remote Sensing Algorithm to Estimate the Surface Energy Balance. *Phys. Chem. Earth Part B Hydrol. Ocean. Atmos.* **2000**, *25*, 147–157. [[CrossRef](#)]
- Su, Z. The Surface Energy Balance System (SEBS) for Estimation of Turbulent Heat Fluxes. *Hydrol. Earth Syst. Sci.* **2002**, *6*, 85–99. [[CrossRef](#)]
- Allen, R.G.; Tasumi, M.; Trezza, R. Satellite-based energy balance for mapping evapotranspiration with internalized calibration (METRIC)—Model. *J. Irrig. Drain. Eng.* **2007**, *133*, 380–394. [[CrossRef](#)]

25. Shuttleworth, W.J.; Wallace, J.S. Evaporation from Sparse Crops—An Energy Combination Theory. *Q. J. R. Meteorol. Soc.* **1985**, *111*, 839–855. [[CrossRef](#)]
26. Kustas, W.P.; John, M. Norman. Evaluation of Soil and Vegetation Heat Flux Predictions Using a Simple Two-Source Model with Radiometric Temperatures for Partial Canopy Cover. *Agric. For. Meteorol.* **1999**, *94*, 13–29. [[CrossRef](#)]
27. Norman, J.M.; Kustas, W.P.; Humes, K.S. Source Approach for Estimating Soil and Vegetation Energy Fluxes in Observations of Directional Radiometric Surface Temperature. *Agric. For. Meteorol.* **1995**, *77*, 263–293. [[CrossRef](#)]
28. Su, Z.; Pelgrum, H.; Menenti, M. Aggregation Effects of Surface Heterogeneity in Land Surface Processes. *Hydrol. Earth Syst. Sci.* **1999**, *3*, 549–563. [[CrossRef](#)]
29. Crago, R.D. Comparison of the Evaporative Fraction and the Priestley–Taylor α for Parameterizing Daytime Evaporation. *Water Resour. Res.* **1996**, *32*, 1403–1409. [[CrossRef](#)]
30. Li, G.; Zhang, F.; Jing, Y.; Liu, Y.; Sun, G. Response of evapotranspiration to changes in land use and land cover and climate in China during 2001–2013. *Sci. Total Environ.* **2017**, *596*, 256–265. [[CrossRef](#)] [[PubMed](#)]
31. Liu, Y.; Zhuang, Q.; Chen, M.; Pan, Z.; Tchebakova, N.; Sokolov, A.; Parfenova, E. Response of evapotranspiration and water availability to changing climate and land cover on the Mongolian Plateau during the 21st century. *Glob. Planet. Chang.* **2013**, *108*, 85–99. [[CrossRef](#)]
32. Rahimi, S.; Gholami Sefidkouhi, M.A.; Raeini-Sarjaz, M.; Valipour, M. Estimation of Actual Evapotranspiration by Using MODIS Images (a Case Study: Tajan Catchment). *Archive. Agron. Soil Sci.* **2015**, *61*, 695–709. [[CrossRef](#)]
33. Hong, Y. Actual Evapotranspiration Estimation for Different Land Use and Land Cover in Urban Regions Using Landsat 5 Data. *J. Appl. Remote Sens.* **2010**, *4*, 041873. [[CrossRef](#)]
34. Allen, R.G.; Pereira, L.S.; Howell, T.A.; Jensen, M.E. Evapotranspiration information reporting: I. Factors governing measurement accuracy. *Agric. Water Manag.* **2011**, *98*, 899–920. [[CrossRef](#)]
35. Degano, M.F.; Rivas, R.E.; Carmona, F.; Niclos, R.; Sanchez, J.M. Evaluation of the MOD16A2 Evapotranspiration Product in an Agricultural Area of Argentina, the Pampas Region. *Egypt. J. Remote Sens. Space Sci.* **2021**, *24*, 319–328. [[CrossRef](#)]
36. Li, Z.; Liu, X.; Ma, T.; Kejia, D.; Zhou, Q.; Yao, B.; Niu, T. Retrieval of the surface evapotranspiration patterns in the alpine grassland–wetland ecosystem applying SEBAL model in the source region of the Yellow River, China. *Ecol. Model.* **2013**, *270*, 64–75. [[CrossRef](#)]
37. Sriwongsitanon, N.; Suwawong, T.; Thianpopirug, S.; Williams, J.; Jia, L.; Bastiaanssen, W. Validation of seven global remotely sensed ET products across Thailand using water balance measurements and land use classifications. *J. Hydrol. Reg. Stud.* **2020**, *30*, 100709. [[CrossRef](#)]
38. Wang, Y.; Liu, Y.; Jin, J. Contrast Effects of Vegetation Cover Change on Evapotranspiration during a Revegetation Period in the Poyang Lake Basin, China. *Forests* **2018**, *9*, 217. [[CrossRef](#)]
39. Gibson, L.A.; Jarmain, C.; Su, Z.; Eckardt, F.E. Estimating Evapotranspiration Using Remote Sensing and the Surface Energy Balance System—A South African Perspective. *Water Sa* **2013**, *39*, 477–484. [[CrossRef](#)]
40. Srivastava, A.; Sahoo, B.; Raghuvanshi, N.S.; Singh, R. Evaluation of Variable-Infiltration Capacity Model and MODIS-Terra Satellite-Derived Grid-Scale Evapotranspiration Estimates in a River Basin with Tropical Monsoon-Type Climatology. *J. Irrig. Drain Eng.* **2017**, *143*, 04017028. [[CrossRef](#)]
41. Autovino, D.; Minacapilli, M.; Provenzano, G. Modelling bulk surface resistance by MODIS data and assessment of MOD16A2 evapotranspiration product in an irrigation district of Southern Italy. *Agri. Wat. Manag.* **2016**, *167*, 86–94. [[CrossRef](#)]
42. Cawse-Nicholson, K.; Braverman, A.; Kang, E.L.; Li, M.; Johnson, M.; Halverson, G.; Anderson, M.; Hain, C.; Gunson, M.; Hook, S. Sensitivity and uncertainty quantification for the ECOSTRESS evapotranspiration algorithm—DisALEXI. *Int. J. Appl. Earth. Obs. Geoinformation* **2020**, *89*, 102088. [[CrossRef](#)]
43. Jung, H.C.; Getirana, A.; Arsenault, K.R.; Holmes, T.R.H.; McNally, A. Uncertainties in Evapotranspiration Estimates over West Africa. *Remote Sens.* **2019**, *11*, 892. [[CrossRef](#)]
44. Baba Jafary, H.; Paymazd, S.; Moghadasi, M. Estimation of Actual Evapotranspiration of Urmia Lake Basin Using SEBS Remote Sensing Algorithm and AVHR Sensor Im-Ages. *Echo Hydrol.* **2015**, *5*, 1285–1296. [[CrossRef](#)]
45. Bagheri, M.H. Remote Sensing Technology Assessment in Basin Water Scale. In *Determining the Purpose of Underground Water Consumption Case Study: Lake Urmia Basin*; Elsevier Ltd.: Amsterdam, The Netherlands, 2011. [[CrossRef](#)]
46. Ziaee, R.; Moghaddasi, M.; Payamzad, S.; Bagheri, M.H. *Estimation and Evaluation of Evaporation from Water Levels Using the SEBS Remote Sensing Algorithm and Comparison with SEBAL Algorithm, Case Study: Lake Urmia*; Elsevier Inc.: Amsterdam, The Netherlands, 2014. [[CrossRef](#)]
47. Vahed, S.Z.; Forouhandeh, H.; Hassanzadeh, S.; Klenk, H.P.; Hejazi, M.A.; Hejazi, M.S. Isolation and characterization of halophilic bacteria from Urmia Lake in Iran. *Microbiology* **2011**, *80*, 834–841. [[CrossRef](#)]
48. Daneshi, A.; Panahi, M.; Masoomi, S.; Vafakhah, M.; Azadi, H. Assessment of Non-Monetary Facilities in Urmia Lake Basin under PES Scheme: A Rehabilitation Solution for the Dry Lake in Iran. *ENVI* **2021**, *23*, 10141–10172. [[CrossRef](#)]
49. Khoshnoodmotlagh, S.; Verrelst, J.; Daneshi, A.; Mirzaei, M.; Azadi, H.; Haghighi, M.; Hatamimanesh, M.; Marofi, S. Trans-boundary Basins Need More Attention: Anthropogenic Impacts on Land Cover Changes in Aras River Basin, Monitoring and Prediction. *Remote Sens.* **2020**, *12*, 3329. [[CrossRef](#)]
50. Al-Ahmadi, F.S.; Hames, A.S. Comparison of four classification methods to extract land use and land cover from raw satellite images for some remote arid areas, Kingdom of Saudi Arabia. *Earth Sci.* **2009**, *20*, 167–191. [[CrossRef](#)]

51. Rawat, J.S.; Kumar, M. Monitoring land use/cover change using remote sensing and GIS techniques: A case study of Hawalbagh block, district Almora, Uttarakhand, India. *Egypt. J. Remote Sens. Space Sci.* **2015**, *18*, 77–84. [[CrossRef](#)]
52. Sun, J.; Yang, J.; Zhang, C.; Yun, W.; Qu, J. Automatic remotely sensed image classification in a grid environment based on the maximum likelihood method. *Math. Comput. Model.* **2013**, *58*, 573–581. [[CrossRef](#)]
53. Kwast, V.H.; De Jong, S.M. Modelling Evapotranspiration Using the Surface Energy Balance System (SEBS) and Landsat TM Data (Rabat Region, Morocco). *EARSeL Workshop Remote Sens. Dev. Ctries.* **2004**.
54. Shunlin, L.; Dongdong, W.; Tao, H.; Yunyue, Y. Remote sensing of earth's energy budget: Synthesis and review. *Int. J. Digi. Earth* **2019**, *12*, 737–780. [[CrossRef](#)]
55. Byun, K.; Liaqat, U.W.; Choi, M. Dual-Model Approaches for Evapotranspiration Analyses over Homo- and Heterogeneous Land Surface Conditions. *Agric. For. Meteorol.* **2014**, *197*, 169–187. [[CrossRef](#)]
56. Farokhnia, A.; Moradi, S.; Delvar, M. Study of Land Use Change in the Urmia Lake Water Shed Based on Landsat- TM Images and Pixel-Based and Object-Based Classification Techniques. *Iran. J. Irrig. Drain.* **2018**, *12*, 823–839.
57. Kamali, M.; Yuneszadeh, S. Analysing Land Use Change within the Lake Urmia Basin Using Satellite Images. *Plan. Resour. Mobilization Unit Urmia Lake Restor. Program* **2015**, 71. (In Persian)
58. Pourmohammadi, S.; Dasturani, M.T.; Mokhtari, M.H.; Rahimian, M.H. Determination and Zoning of Actual Evapotranspiration by Remote Sensing Technique and Sabal Theme Algorithm (Case Study: Manshad Watershed in Yazd Province). *Watershed Manag. Sci. Eng.* **2011**, *4*, 21–30.
59. Jahangir, M.H.; Arast, M. Remote Sensing Products for Predicting Actual Evapotranspiration and Water Stress Footprints under Different Land Cover. *J. Clean. Prod.* **2020**, *266*, 121818. [[CrossRef](#)]

Disclaimer/Publisher's Note: The statements, opinions and data contained in all publications are solely those of the individual author(s) and contributor(s) and not of MDPI and/or the editor(s). MDPI and/or the editor(s) disclaim responsibility for any injury to people or property resulting from any ideas, methods, instructions or products referred to in the content.